PCCP

Adsorption and exchange reactions of iodine molecules at the alumina surface: modelling alumina-iodine reaction mechanisms

Journal:	*Physical Chemistry Chemical Physics*
Manuscript ID	CP-ART-12-2021-005924.R1
Article Type:	Paper
Date Submitted by the Author:	14-Mar-2022
Complete List of Authors:	Miller, Kelsea; Texas Tech University System, de Rezende, Armando; Texas Tech University Aquino, Adelia; Texas Tech University Tunega, Daniel; University of Natural Resources and Life Sciences Vienna, Institute for Soil Research Pantoya, Michelle; Texas Tech University Department of Mechanical Engineering,

ARTICLE

Adsorption and exchange reactions of iodine molecules at the alumina surface: modelling alumina-iodine reaction mechanisms

Received 00th January 20xx,
Accepted 00th January 20xx

DOI: 10.1039/x0xx00000x

Kelsea K. Miller[a], Armando de Rezende[a], Adelia J. A. Aquino*[ab], Daniel Tunega*[b], and Michelle L. Pantoya*[a]

Harnessing aluminum oxidation energy requires navigating the particle's passivation shell composed of alumina. The shell is a barrier to aluminum oxidation but can also exothermically react with halogenated species and therefore contribute to the overall energy generated during aluminum particle combustion. Fluorination reactions with alumina have been studied because fluorine is abundant in binder formulations that commonly surround aluminum particles in an energetic mixture. However, iodine has emerged as an alternative halogenated-based binder or oxidizer because iodine gas provides ancillary benefits such as chemical neutralization of biological agents or sterilization of contaminated environments. This study used density functional theory (DFT) calculations to evaluate potential reaction pathways for aluminum-iodine combustion. Relative to fluorinated fragments such as HF and F^-, the adsorption energies associated with HI and I^- are nearly triple the exchange reaction energy available from fluorination reactions with alumina (-189 and -278 kJ/mol for HI and I^-, respectively). However, exchange reactions between iodinated species and the alumina surface are energetically unfavorable. These results explain that through adsorption, alumina surface exothermic reactions with iodine are more energetic than with fluorine fragments. Experiments performed with differential scanning calorimetry (DSC) confirm the higher magnitude of energy generated for iodination compared with fluorination reactions with alumina. Additionally, strong adsorption energies can promote synthesis of new shell chemistries. Adsorption in solution will promote alumina dissolution and iodine precipitation reactions to produce hydroxyl complexes and iodinated species synthesized on the surface of the particle, thereby replacing alumina with alternative passivation shell chemistry.

Introduction

The aluminum fuel particle is a multi-layered composite composed of a crystalline aluminum core surrounded by an amorphous alumina passivation shell which is further surrounded by a loosely bonded hydration layer shown in Fig. 1. The native oxide layer protects the pyrophoric core from spontaneous reaction with surrounding oxygen. The hydroxylated outer layer provides active sites to promote exothermic reactions with alumina. The alumina surface reactions increase energy generation potential within energetic formulations. Crouse et al. [1] and Miller et al. [2] encapsulated nanoscale aluminum particles (nAl) with fluoropolymers that generated additional energy from alumina fluorination reactions upon combustion. Pantoya and Dean [3] showed that for nanoscale particles the surface exothermic reaction between alumina and fluorinated species measurably contributed to the overall energy generated during a reaction. All of these studies suggest a new way of thinking: the alumina's surface exothermic reaction could be used to tailor energy release of the aluminum fuel particle.

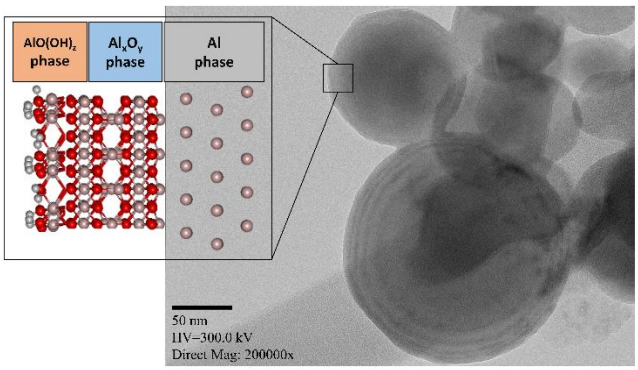

Fig. 1 TEM micrograph of commercial nAl with inset showing schematic of interfaces between Al/AlO/AlO(OH) phases.

Padhye et al. [4] showed a linear relationship between increased alumina surface fluorination reactions and increased main aluminum oxidation reactions. They recognized that aluminum particles are often in direct contact with fluorinated binders that hold together an energetic mixture. Padhye et al. [5] also showed that terminal -OH bonds on the surface of the alumina's outer shell are active sites for exothermic reactions with fragmented fluorinated species that are common decomposition products from the

[a] Department of Mechanical Engineering, Texas Tech University, Lubbock, Texas 79409, USA
[b] Institute for Soil Research, University of Natural Resources and Life Sciences, Peter-Jordan-Strasse 82, Wien A-1190, Austria
[c] Corresponding authors: michelle.pantoya@ttu.edu; adelia.aquino@ttu.edu; daniel.tunega@univie.ac.at

fluorinated binders. Density functional theory (DFT) calculations were coupled with experimental enthalpy measurements to confirm that increased surface energy could be achieved from alumina surfaces with higher concentrations of terminal -OH bonds. In turn, greater surface exothermic energy resulted in more complete combustion of the core aluminum.

While fluorine is abundant in binder formulations, other halogenated species also provide opportunities to capitalize on surface exothermic reactions. Iodine oxides have been widely studied as an appealing solid oxidizer owing to the abundance of iodine [6]. The production of gas phase iodine species can supplement a reaction by providing a chemical neutralization strategy [7]. Iodine gas can neutralize spore forming bacteria, such as Anthrax, and effectively sterilize an otherwise contaminated environment. The appeal of carrying iodine gas in solid form that can be gasified upon reaction prompted the development of iodinated binders that could replace or be used in conjunction with the more common fluorinated binders [8]. Additionally, other researchers synthesized iodine rich solid oxidizers that could also be added to energetic formulations. One promising iodine rich oxidizer is aluminum iodate hexahydrate (AIH) $[Al(H_2O)_6(IO_3)_3(HIO_3)$. Not only does AIH have a high oxygen balance (+20) but AIH is also highly reactive when combined with aluminum fuel particles [9].

Early studies on the interaction between aluminum particles and iodine oxides revealed almost all intermediate reactions are exothermic. Farley et al. [10] used DFT to calculate formation energies of several intermediate reactions involving iodine fragments with the alumina surface. Mulamba et al. [11] used equilibrium thermal analysis to examine surface reactions between iodine pentoxide and aluminum fuel particles. They showed a sequence of iodine-aluminum reactions experimentally that matched DFT predictions for enthalpy made by Farley et al.[10]. The exothermic potential available in surface reaction provides motivation for further exploring the interface between iodine suboxides and the alumina surface surrounding aluminum particles.

The goal of this study is to identify structure and energetics for specific iodine – alumina surface interactions. The goal was accomplished using DFT calculations compared with experimentally measured enthalpies using differential scanning calorimetry (DSC). This goal extends previous work because the calculations involve iodine suboxide fragment species applicable to a wide range of decomposition products from iodine-based oxidizers. The assumption is that the four primary decomposition fragments from iodinated oxidizers are I_2, IO, HI, and I^- and these species can react with different hydroxyl coordinations on the alumina surface. Five types of surface hydroxyl groups were identified at γ-Al_2O_3 surfaces. The -OH sites differ by the coordination and linking to two types of Al atoms in γ-Al_2O_3: i.e., octahedrally (Al_{VI}) and tetrahedrally (Al_{IV}) coordinated. Fig. 2 shows detailed binding of these five -OH sites: two terminal -OH sites Al_{IV}-OH and Al_{VI}-OH (Ia and Ib), two bridge -OH sites Al_{IV}-OH-Al_{VI} and Al_{VI}-OH-Al_{VI} (IIa and IIb), and one edge -OH site $(Al_{VI})_3$-OH (III) [12].

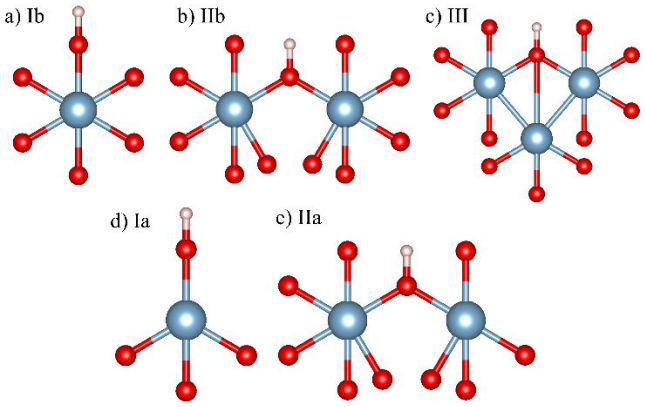

Fig. 2 Structural details of the five -OH reaction sites of the γ-Al_2O_3 surface. Aluminum atoms are in blue, oxygen in red, and hydrogen in pink. Notation of -OH groups according to reference [12].

The DFT analysis reveals the most reactive surface -OH sites that can strongly adsorb iodinated species, promote surface iodination reactions, and quantify the magnitude of the exothermic energy from the adsorption process. The experimental measurements of reaction enthalpy support the DFT calculations. Focusing on iodine surface reactions enables a comparison to previously published fluorination surface reactions to identify reaction pathways that are the most energetic for future synthesis and development of metal fuel particles.

DFT Calculations

Two different physical-chemical processes at the alumina surface were examined to understand the energy of its interactions with iodine molecules. The first calculations were for adsorption energy and the second were for exchange reactions.

Adsorption Energy

DFT calculations were performed to estimate the adsorption energy (ΔE_{ads}) of the hydroxyl surface complexes formed by the adsorption of I_2, IO, HI, and I^- at different active sites on the alumina surface (Fig. 2). ΔE_{ads} was calculated as a difference between the total energy of product (surface complex) and two reactants according to Reaction (1) where R is equal to I_2, IO, HI molecules, or I^- anion.

$$\gamma\text{-}Al_2O_3\text{-}OH + R \rightarrow \gamma\text{-}Al_2O_3\text{-}OH\cdots R \qquad (1)$$

The periodic slab models of γ-A_2O_3 surfaces were created based on the single crystal X-ray diffraction experimental bulk structure of γ-Al_2O_3 as detailed previously [13]. Two slab models were required to model five different sites at the (111) surface terminated by A or B planes. Specifically, Ia and IIa sites in the slab are terminated with plane A (model slab_A), and Ib, IIb, and III sites in the slab are terminated with plane B (model slab_B). Fig. 2 shows all five OH sites with a detailed Al coordination., Fig. S1 in the Supplementary Information displays complete structures of two slab models of γ-Al_2O_3 surfaces and Table S1 collects corresponding structural data. Both slab models contained 120 atoms being periodic in the surface directions with a vacuum of about 35 Å in the normal direction to

minimize interactions between the molecules and the surface in the upper projection. The thickness of the slab models (counted as the distance between terminal atomic planes of O atoms, Fig. S1) was about 6.8 Å (slab_A), and 6.6 Å (slab_B), respectively. The initial distance between adsorbent and adsorbate was set to ~3.5 Å for all cases except for the vertical orientation of the -HI molecule that was set to 1.5 Å (see Supplementary Information, Fig S2-h) as the H atom of HI molecule points towards the surface O atom, it is expected to form a hydrogen bond. In case of I^-, cluster models for all five sites were used because periodic slab models were unsuitable to predict adsorption energy for charged systems. Similar cluster models developed from the slab models are described in detail in our previous work [13].

Exchange Reaction Energy

In addition to adsorption energies, DFT calculations were extended to evaluate exchange reactions between surface hydroxyl sites with I^- and HI. Particularly, in exchange reactions the -OH site at the surface was replaced by iodine according to Reaction (2) where X = H for HI (i.e., the exchange reactions were only performed for HI and I^-).

$$Al_2O_3{-}OH + X{-}I \rightarrow Al_2O_3{-}I + X{-}OH \quad (2)$$

Reaction energy, ΔE_r, is calculated as the sum of total electronic energies of products minus the sum of total electronic energies of reactants, respectively. The iodine surface reactions described by Reaction (2) are like surface fluorination reactions studied previously[5,13].

Note that the calculations for the exchange reactions in Reaction (2) were not performed for site III $(AlVI)_3$-OH because the hydroxyl group is bound to three aluminum atoms in this site. Therefore, to break all three bonds is a process highly energetically unfavorable, thus improbable.

DFT Computational Details

Prior to calculations, geometry optimizations were performed for the pristine slab and cluster models, isolated iodine species, and the formed complexes or reactants. In case of slab adsorption models, I_2, IO and HI were optimized with different initial positions to find the most stable configurations. Details about these initial positions are shown in Supplementary Information (Figure S2). In short, I_2, IO and HI were placed in both horizontal and vertical orientations towards each active site. In the case of the asymmetric IO and HI species, two vertical and two horizontal structures changing the position of the iodine, oxygen, or hydrogen atoms related to the active site were calculated to determine the most stable geometries of the formed complexes.

DFT calculations for periodic neutral slab models were performed with the VASP program suite [14–17] using projector augmented wave (PAW) pseudopotentials [18], with the Perdew–Burke-Ernzerhof (PBE) functional [19]. The cutoff energy for plane-waves was set to 400 eV. The SCF energy convergence was set to 10^{-5} eV and the convergence criterium for geometry optimization was also set to 10^{-5} eV. All systems were calculated in Γ-point due to the large size of the unit cells for the slab models. The cluster calculations were performed using the Turbomole program [20] with the PBE functional and the def2-TZVP basis set [21,22]. Note that the energy-consistent Stuttgart/Cologne scalar relativistic pseudopotential ECP28 was used for iodine [23] and its valence electrons were treated with def2-TZVP basis set. The Grimme DFT-D3 correction for dispersion interactions was used throughout all slab and cluster calculations [24].

Experimental

Experiments focused on differential scanning calorimetry and thermal gravimetric analysis (DSC-TGA) to quantify heat flow and mass change under equilibrium conditions. Samples were prepared by immersing commercial nano-scale Al particles (nAl) in an iodic acid solution to form nAl particles decorated with iodates including AIH. X-ray Diffraction (XRD) patterns were also obtained to confirm the composition of species in each sample prior to the DSC-TGA analysis. The decomposition mechanism for AIH and HIO_3 is discussed such that key exothermic surface reactions including IO, I_2, HI, and I^- species can be realized.

Sample Preparation

The aluminum particles were procured from Novacentrix (Austin, TX) with an 80 nm average diameter including a 4-6 nm alumina passivation shell. In order to partially remove and subsequently replace the Al_2O_3 shell with AIH, 150 mg of nAl powder was immersed in an aqueous iodic acid solution. The solution was composed of iodopentoxide (I_2O_5) dissolved in ChromeAR™ water. This procedure is detailed elsewhere [25] but described briefly below.

The two samples were identified as Al@AIH34 and Al@AIH30. The designations of 34 and 30 represent AIH concentration discussed below in the composition analysis. Initial concentrations of I_2O_5 powder were determined from a balanced chemical equation, Reaction (3), for an equivalence ratio (ER) of 1.1. Next, the amount of water used for mixing the aqueous iodic acid solution was determined from a I_2O_5 to water ratio of 1:1.

$$10Al + 3I_2O_5 \rightarrow 5Al_2O_3 + 3I_2 \quad (3)$$

The formation of AIH was shown to be dependent on the pH of the iodic acid and nAl solution by Smith et al. [25] A polarization mechanism that hydrates the Al_2O_3 surface to $[Al(H_2O)_6]$ was proposed as an essential kinetic step in AIH formation. Smith et al. [26] also demonstrated a dependence on time for forming AIH. Allowing nAl to stay in the iodic acid for extended durations lead to higher AIH concentrations. However, little control was shown between batch variations, i.e., 78 wt% AIH was reported in Smith et al. [26] and only 6-15% reported in Gottfried et al.[9]. In an attempt to mitigate batch variations and facilitate chemical interaction between the nAl and acidic iodic solution, sample containers were sealed in Paraffin for 24 hours prior to exposure to air drying.

Fig. 3 shows SEM images of the two samples and illustrates the morphology of the composite particles. The crystalline, granular structure of the surface is consistent with the morphology of AIH and HIO_3, while the core remains Al.

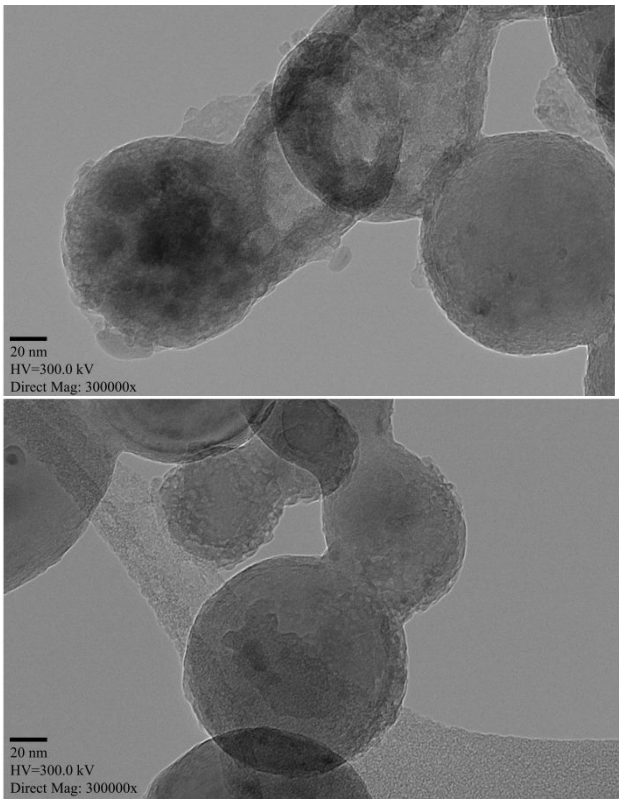

Fig. 3 Iodinated crystallization on the surface of Al@AlH34 (top) and Al@AlH30 (bottom). Similar structures appear for both samples.

Compositional Analysis

Powder XRD data were collected on a Rigaku MiniFlex II powder diffractometer operating in continuous θ-2θ mode from 3°-60° 2θ with Bragg-Brentano geometry. Powders were mounted on a zero-background holder and the X-ray source was Cu Kα radiation (λ=1.5418 Å) with a current of 15 mA and an anode voltage of 30 kV. The step size was 0.02° with a collection rate of 2°/min. Diffraction intensities were captured with a D/teX Ultra 1D silicon strip detector. Qualitative and quantitative analyses were conducted using whole pattern fitting Rietveld refinement with MDI Jade V9.1.1 software. Three phases were identified: aluminum, delta hydrogen iodate (δ-HIO_3), and AlH shown in Fig. 4 with peaks labelled and wt.% composition indicated.

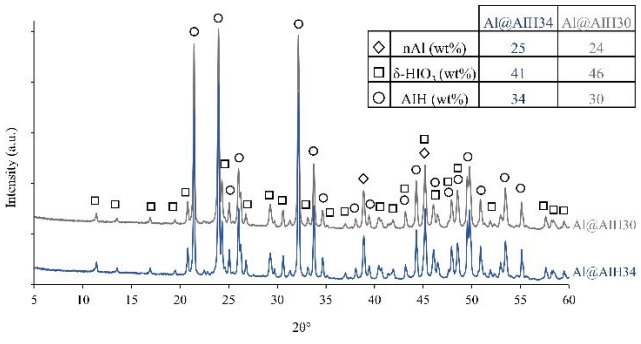

Fig. 4 The XRD patterns of Al@AlH samples with identified crystalline species. The weight concentration from whole pattern fitting Rietveld Refinement analysis of each pattern is provided in table inset, with R-values of 4.81 and 5.04 for nAl@AlH34 and nAl@AlH30, respectively.

Equilibrium Thermal Analysis

Differential scanning calorimetric and thermogravimetric analysis were conducted using a NETZSCH STA 449 F3 Jupiter simultaneous thermal analyzer (STA). The STA was calibrated with indium and calcium oxalate for the DSC and TG, respectively. The melting temperature of indium and weight loss of calcium oxalate matched the literature value with an uncertainty within ± 1%. For each experiment, powder mass was maintained at 3.5 mg and loaded in a lidded alumina crucible. A small pin hole in the lid of the crucible allows gas to escape and therefore register mass change. An initial argon (Ar) gas purge removed residual oxygen in the instrument lines. All experiments were performed at a heating rate of 10 °C/min in an Ar environment for temperatures from 30 to 800°C. All data were processed with NETZSCH Proteus software to determine onset temperature and enthalpy for fluctuations in heat flow.

Results

Density Functional Theory Results

Optimized Structures. Figs. 5 and 6 display the most stable configurations of all combinations from the geometry relaxation for both slab and cluster calculations, respectively. Important interatomic distances are also provided in Figs. 5 and 6. Fig. 5 shows optimized structures for adsorption reactions while Fig. 6 shows optimized structures for exchange reactions. Figures S3-S7 in Supplementary Information present all optimized configurations for each I-bearing moiety on the γ-Al_2O_3 active surface sites prior to the optimization procedure for more detailed information.

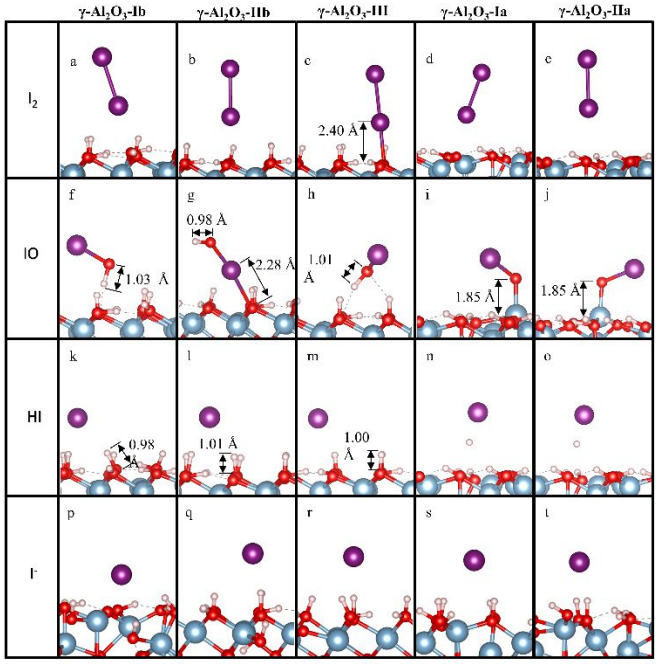

Fig. 5 The most stable structures of the active hydroxyl sites Ib, IIb, III, Ia, IIa (shown in columns, respectively) on the γ-Al_2O_3 surface for the adsorption reactions with iodine species that are indicated in each row. Selected interatomic distances from slab model calculations are also shown except for the last row for anion iodine interactions (i.e., p-t) for which the cluster model was used in the computations.

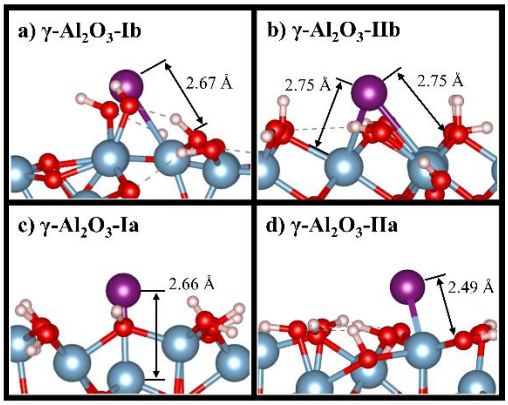

Fig. 6 Optimized structures of the active sites Ia, IIa, Ib, and IIb on the γ-Al_2O_3 surface from exchange reactions with HI and I^- including selected interatomic distances using cluster models.

Adsorption Reactions. Table 1 shows calculated adsorption energies for all models investigated. In all cases, iodine species strongly adsorb to surface -OH sites. The interactions of I_2 with the active sites of γ-Al_2O_3 are noncovalent (physisorption). The interactions of IO are much stronger than in case of I_2, and are chemisorbed and/or accompanied by a proton transfer. Particularly, for sites Ia and IIa (I)O-Al bonds are 1.9 Å. The Al atom that bonds with IO is partially withdrawn from the tetrahedral position (Al_{IV}), as in the case of terminal -OH (i.e., Ia site) a neighboring Al_{IV} is close to the Ia site. On the other hand, formation of HIO by a proton transfer from the surface is observed for sites Ib, IIb, and III, respectively. The formed HIO is bound to the surface by hydrogen bonds (Ib and III sites). However, for IIb, HIO forms a very strong interaction with the surface via direct I-O_s binding, where O_s is the oxygen atom from one surface -OH group.

For deprotonation of HI in sites Ib, IIb, and III (Fig. 5: k, l and m), the proton is abstracted by oxygen in the alumina surface and calculated adsorption energies are very high (Table 1). Conversely, for Ia and IIa, no proton transfer was observed, and corresponding adsorption energies are much lower than Ib, IIb, and III. The HI molecule forms hydrogen bonds with surface -OH groups where HI is the proton donor and surface -OH sites are proton acceptors. In the case of a charged complex such as I^-, surface -OH groups interact as proton donors with I^- through strong hydrogen bonding with H···I distances in a range of 2.0 -2.8 Å (**Fig. 5**: p-t).

The interactions of I^- species are not solely with the active -OH site but also due to the surface morphology and arrangement of different -OH surface sites because neighboring -OH groups can cooperate in the adsorption. For example, this is the case for IIb (Fig. 5 q) where the interaction of I^- is observed along with the hydrogen atom from neighboring III resulting in a IIb adsorption energy of -275.25 kJ/mol for I^- adsorption. However, I^- reconnects to -OH on III in the vicinity of IIb (distance of ~3 Å). Stronger adsorption (i.e., higher adsorption energy in absolute value) achieved in the calculation for IIb compared to III can be explained by a cooperative effect of IIb and III -OH sites interacting with the I^- anion.

The ΔE_{ads} values calculated according to Reaction (1) presented in Table 1 show that all the adsorption reactions are energetically strongly favorable. Ia (Al_{IV}-OH) and IIa (Al_{IV}-OH-Al_{VI}) are the less reactive sites for all adsorption processes of iodine species. Note that for these two sites reactions with IO and I^- are more energetic. In the reaction with IO, the oxygen atom of this molecule forms a covalent bond (chemisorption) with the Al atom from the γ-Al_2O_3 surface (Fig. 5 i and j). The strongest adsorption reactions are between site IIb (Al_{VI}-OH-Al_{VI}) and I^- ($D E_{ads}$ = -278.25 kJ/mol), followed by site III ((Al_{VI})$_3$-OH) and I^- ($D E_{ads}$ = -228.91 kJ/mol), and HI ($D E_{ads}$ = -226.85 kJ/mol). In the case of HI, a chemisorption process is observed for sites Ib, IIb, and III, in which the hydrogen atom from HI is abstracted by an oxygen atom from the surface -OH groups (note that for III, the abstraction of H^+ is by IIb in the vicinity of III). The adsorption processes labelled as physisorption, and chemisorption were categorized not only on the base of energetic criteria but also on geometrical. In chemisorbed cases some original bonds were broken, and some new bonds were created (e.g., proton transfer from iodine species to surface formed new surface OH group).

Table 1 Adsorption energies and final processes in the adsorption reaction of iodine species reacting with five -OH active sites of γ-Al_2O_3 surface.

Species	Active sites	ΔE_{ads} (kJ/mol)	Final reaction
I_2	γ-Al_2O_3-Ib	-64.63	Physisorption
	γ-Al_2O_3-IIb	-60.75	Physisorption
	γ-Al_2O_3-Ia	-54.01	Physisorption
	γ-Al_2O_3-IIa	-33.12	Physisorption
	γ-Al_2O_3-III	-110.72	Physisorption
IO	γ-Al_2O_3-Ib	-109.55	Chemisorption/HIO
	γ-Al_2O_3-IIb	-187.30	Chemisorption/HIO
	γ-Al_2O_3-Ia	-97.66	Chemisorption/Al-O-I
	γ-Al_2O_3-IIa	-115.52	Chemisorption/Al-O-I
	γ-Al_2O_3-III	-141.82	Chemisorption/ HIO
HI	γ-Al_2O_3-Ib	-167.53	Chemisorption/HI
	γ-Al_2O_3-IIb	-188.53	Chemisorption/HI
	γ-Al_2O_3-Ia	-59.81	Physisorption
	γ-Al_2O_3-IIa	-60.30	Physisorption
	γ-Al_2O_3-III	-226.85	Chemisorption/HI
I^-	γ-Al_2O_3-Ib	-187.06	Physisorption
	γ-Al_2O_3-IIb	-278.25	Physisorption

γ-Al_2O_3-Ia	-183.51	Physisorption
γ-Al_2O_3-IIa	-120.94	Physisorption
γ-Al_2O_3-III	-228.91	Physisorption

Exchange Reactions. Table 2 summarizes the energy results for the exchange reactions, i.e., Reaction (2), for four -OH sites on the γ-Al_2O_3 with I^- and HI. These two iodine species were selected to understand if I^- species can react by a similar mechanism as F^- species shown previously [4] with four -OH sites on γ-Al_2O_3. Thus, the purpose was to see if I^- can replace surface -OH groups to make direct Al-I binding as F^- replaces -OH to make direct Al-F binding.

The exchange reactions are not energetically favorable. For all -OH sites, reaction energy (ΔE_r) both with HI and I^- are highly positive (except Ib and HI for which the -OH group is bound only with one aluminum atom and shows the lowest positive reaction energy for both I^- and HI). In contrast, for reactions of IIa (Al_{IV}-OH-Al_{VI}), where two Al-OH bonds are broken, the reaction energies are the highest.

The results indicate that direct chemical replacement of -OH sites by I^- is not probable (in contrast to F^- investigated by Padhye et al.[5]). The observation that iodination reactions are not energetically favorable compared with fluorination reactions (Reaction 2) can be explained by a large ionic radius of I^- such that forming a direct Al-I bond is not preferred due to steric repulsion of neighboring -OH sites and much stronger Al-OH bonds compared to potential Al-I bond. Al-I bond distances are ~2.5-2.8 Å (Fig. 6). Thus, this bond is much weaker than the strong Al-OH bond in the range of 1.73 to 1.88 Å.

Table 2 Reaction energies of final processes in the exchange chemical reaction (Eq. 2) of OH replacement by I^- and HI reacting with four different -OH active sites of g-Al_2O_3 surface.

Species	Active sites	ΔE_r (kJ/mol)	Final reaction
I^-	γ-Al_2O_3-Ib	382.78	Al_2O_3–OH+I^- → Al_2O_3–I+OH^-
	γ-Al_2O_3-IIb	538.70	
	γ-Al_2O_3-Ia	489.57	
	γ-Al_2O_3-IIa	577.36	
HI	γ-Al_2O_3-Ib	10.73	Al_2O_3–OH+HI → Al_2O_3–I+H_2O
	γ-Al_2O_3-IIb	166.65	
	γ-Al_2O_3-Ia	117.52	
	γ-Al_2O_3-IIa	205.32	

Experimental Results

The nAl particle shells were altered using an iodic acid solution to transform the alumina surface into mainly AlH and HIO_3 (Fig. 3a and b). Both AlH and HIO_3 decompose into iodinated fragments, such that the DFT analysis summarized in Tables 1 and 2 can be extended toward experimental data. The decorated nAl particles were examined for mass loss and heat flow with data shown in Fig. 7a and b, respectively.

Figure 7a indicates three steps of mass loss. A summary of endothermic and exothermic events is provided in Fig. 7b. The first step of mass loss agrees with previous work [27,28] and corresponds with decomposition of the water ring in AlH beginning at 110 °C in nAl@AlH30 and 120 °C in Al@AlH34. Reactions (4)-(7) show intermediate reactions in the AlH decomposition process with removal of water and pronated species as the first step. The phase of each species is indicated such that mass loss can be ascribed to the vapor phase species in the reactions.

$$[Al(H_2O)_6](IO_3)_3(HIO_3)_2 \rightarrow Al(IO_3)_3(HIO_3)_2 + 6H_2O_{(v)} \quad (4)$$

$$Al(IO_3)_3(HIO_3)_2 \rightarrow Al(IO_3)_3(I_2O_5) + H_2O_{(v)} \quad (5)$$

$$Al(IO_3)_3(I_2O_5) \rightarrow Al(IO_3)_3 + \frac{2}{5}I_{2\,(v)} + O_{2\,(v)} \quad (6)$$

$$Al(IO_3)_3 \rightarrow \frac{1}{2}Al_2O_3 + \frac{3}{2}I_{2\,(v)} + \frac{15}{4}O_{2\,(v)} \quad (7)$$

Mass loss occurring in the first step (onset 112 °C for Al@AlH30 and 120 °C for Al@AlH34) corresponds to the endothermic event (labelled 1) in Fig. 7b. Decomposition of HIO_3 follows with an onset 332-337 °C (i.e., Reaction (5)) and corresponds to the first indication of an exothermic pre-ignition reaction (PIR), i.e., labelled 2 in Fig. 7b. Because the PIR is exothermic, the DFT results in Tables 1 and 2 suggest that the PIR results from adsorption reactions with decomposing iodine species and any remaining Al_2O_3 shell, but not exchange reactions. Another possibility is that the initial Al_2O_3 shell is completely consumed in the formation reactions for AlH and HIO_3, such that upon AlH and HIO_3 decomposition, the pyrophoric Al core is exposed thereby facilitating exothermic reactions. The observation in Fig. 7b of a slow and constant increase in heat flow suggests that the pyrophoric Al core is supplying a consistent source for exothermic heat flow.

The third step of mass loss is also exothermic (labelled 3 in Fig. 7b) with an onset temperature ranging from 422-427 °C and corresponds to a second exothermic peak that may involve iodine-oxide fragments reacting with the particle surface. The fourth step begins at 463-465 °C and coincides with a larger exothermic reaction that may correspond with consumption of the Al core and liberation of gas phase species (see Fig. 7a and the exotherm labelled 4 in Fig. 7b). At the Al melting temperature of 660°C, a very small endotherm is observed suggesting that the Al was nearly completely consumed in the low temperature (i.e., < 660°C) reactions. The marginally small indication of melting is also consistent with the upward trend in the heat flow data (Fig. 7b) indicating exothermic energy generated nearly continuously throughout the equilibrium experiment.

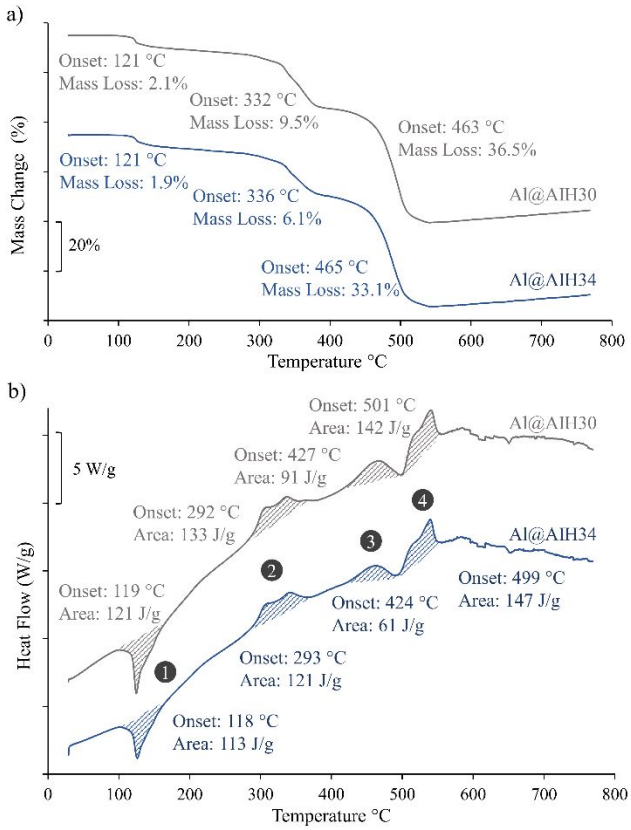

Fig. 7 (a) Mass loss curves with onset temperatures and percentages indicated. (b) Heat flow curves in an argon environment at 10 °C/min heating rate. Curves are shifted vertically for ease of comparison in both figures.

All nAl@AlH samples exhibit an endothermic reaction followed by three exothermic reactions. The endothermic reaction is attributed to the decomposition of the water ring in the AlH molecular structure at 110 °C [9] that occurs between 110 and 120 °C [27,28]. While the exothermic heat flow gradually increases, three peaks are noteworthy. The events labelled 2 and 3 may correspond with surface reactions while the largest peak labelled 4 may correspond with consumption of remaining core Al. All of this exothermic behavior is suggestive that the Al_2O_3 passivation shell is consumed or compromised. Without the shell barrier, the core Al more easily reacts with iodate fragments producing energy and exhibiting the gradual increase in heat flow seen in Fig. 7b. When compared to a mixture of pure AlH particles combined with nAl particles in Kalman et al. [29], the decorated nAl particles (nAl@AlH) here all have earlier onset temperatures for exothermic reactions revealing the limiting effects of the alumina shell.

Discussion

Calculated adsorption energies of I-species show very strong adsorption at γ-Al_2O_3 surfaces with five different -OH sites (Table 1). Exchange reactions at γ-Al_2O_3 surfaces with I^- and HI are energetically unfavorable (Table 2) due to very high positive reaction energies. In contrast, DFT calculated exchange reaction energies for similar reactions with F^- and HF and the same -OH sites on γ-Al_2O_3 [5,13] indicate fluorination surface reactions are favorable and exothermic. A direct comparison between the results here and those found for F^- and HF is summarized in Fig. 8.

The overall characteristics of the exchange reactions in Fig. 8 are similar. The most energetically favorable reactions for fluorinated species occur at γ-Al_2O_3 Ib and Ia surfaces (terminal hydroxyl coordination) [5]. For I^- species, all reaction energies are positive and there are no energetically favorable reactions. For I^- species, adsorption reactions are up to three times more energetically favorable than F^- species exchange reactions. Therefore, surface adsorption reactions with iodine should produce measurably more heat than with fluorine.

Another consideration is that the strong adsorption energies of iodine species shown in Fig. 8 can enhance the dissolving process of γ-Al_2O_3 surfaces in an acidic environment. During the synthesis of AlH on the nAl particles, the strong adsorption reactions in an acidic environment would be followed by precipitation that would explain formation of a thin AlH layer formed at the surface (see Fig. 3). This acid-base precipitation reaction is different from those in which Al_2O_3 surfaces are functionalized by fluorocarbon species through carboxylic acid exchange reactions[1,30] that are energetically favorable. In the case of fluorinated self-assembled monolayers (SAM), the alumina shell remains intact with fluorocarbons attached. In the case of AlH formation, new iodinated shell chemistries replace (or partially replace) the existing alumina shell. By reducing or mitigating the alumina shell, the diffusion barrier is reduced and exothermic reactions with the core can proceed with less resistance.

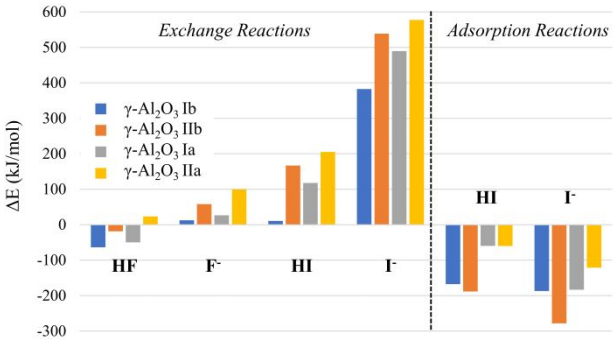

Fig. 8 Comparison of exchange reaction energy (Eq. 2) for F^- [5] and I-species (this study) for four γ-Al_2O_3 surface sites.

To expand the DFT results toward experimental data, a summary of halogenated oxidizers interacting with Al_2O_3 on nAl particle surfaces is presented in Table 3. The distinction between iodinated and fluorinated oxidizers is a measurable increase of the PIR and decrease in onset temperature for iodinated oxidizers.

Table 3 Comparison of exothermic PIR energy and onset temperature for various halogenated surface reactions with alumina.

Literature	Reaction Description	PIR (J/g)	Onset Temperature (°C)
Pantoya and Dean [3]	Various particle sizes of Al_2O_3 mixed with PTFE	11-36	372-418
Padhye et al. [5]	80nm Al with amorphous or crystalline Al_2O_3 shells mixed with PTFE	36-64	428-435
McCollum et al. [31]	Self-assembled monolayer of PFPE over nAl particles with amorphous Al_2O_3 shells	7-30	313-316
Mulamba et al. [11]	Mixtures of Al_2O_3 with I_2O_5 and nAl with I_2O_5	14-20	300-318
Smith et al. [32]	Mixture of 80nm Al and I_2O_5 dispersed in non-polar and polar carrier fluids	58-183	288-367
Kalman et al. [29]	Mixture of 80nm Al and AlH	101	274
Bhattacharia et al. [33]	80nm Al particle coated with AlH and β-HIO_3	135	280
This study	80nm nAl coated with AlH and δ-HIO3 at two weight concentrations	101-133	290

The experimentally observed exothermic energy in surface reactions (PIR) with iodinated species is measurably higher than fluorinated species. The DFT calculations in Tables 1 and 2 suggest that iodine-alumina interactions are adsorption and not exchange reactions. In fact, from the data in Table 3, the average fluorinated PIR energy is 30 J/g and the average iodinated PIR from AlH decomposition is 118 J/g, which is a 293% increase and compares well to the relative increase of 300% resulting from the DFT adsorption calculations.

However, after adsorption, further processes differ for F^- and I^- species. In the case of F^- species, the aluminum fluorination reactions continue because exothermic exchange reactions facilitate further bond breaking. For I^- species, the continuing processes are different. In iodic acid, strong adsorption would promote dissolving the Al_2O_3 surface and facilitate formation of $Al(H_2O)_6$ complexes that can further precipitate in a reaction with IO_3 anions forming AlH. The highly energetically unfavorable exchange reactions with iodine and the Al-OH surface help explain why the formation of AlH is favored in an iodic acid solution. More precisely, iodine species interact with the hydroxylated alumina surface to promote AlH formation rather than consumption of core Al. Continuous exothermic heat flow in Fig. 7b suggests iodate species consumed the original alumina shell such that when the iodate species decompose, the pyrophoric Al core is exposed to oxidizing species and continuously liberates exothermic energy. Another possibility is that the transformed or partially transformed shell includes defect sites that facilitate Al core oxidation throughout the equilibrium reaction. Wren et al.[34] propose a defect mechanism for the growth of an FeI_xO_y layer on stainless steel surfaces resulting from I_2 gas absorption. They explain that accelerated absorption reactions result in many defect sites that act as a semi-conductor facilitating migration of oxygen and iodine gas to the metal iron core. In a similar way, oxygen may diffuse through a defected shell barrier and into core aluminum resulting in a continuous rise in exothermic heat flow measured in Fig. 7. In fact, other studies on aluminum nitride (AlN) substrates for improved semi-conducting materials have also shown similar results.[35,36] Dopants and impurities have been used to promote bonding mechanisms towards crystallization of AlN and directly support the credibility of the physical mechanism revealed in the present study.

Conclusions

Density functional theory (DFT) calculations of surface adsorption and exchange reactions between iodinated species and the alumina surface surrounding aluminum particles were performed. The results show that all types of surface hydroxyl groups on γ-Al_2O_3 surfaces are energetically very favorable for adsorption of all iodine species, but not favorable for exchange reactions. The calculations show that adsorption energies are highest for HI and I^- in the range of -60.0 to -278 kJ/mol, followed by IO (-98 to -187 kJ/mol), and I_2 (-33 to -111 kJ/mol). The calculated exchange reaction energies of replacement of OH group by halogen species show the reaction of I^- and HI are extremely energetically unfavorable in contrast to previous work that showed F^- species surface reactions are favorable.

Results from the DFT analysis indicate two important findings observed in experiments. First, alumina surface reactions with I-species on aluminum particles that exhibit high exothermic energy result from adsorption reactions and cannot occur from exchange reactions. Second, the release of very high adsorption energies from iodine species with Al particles can enhance dissolution of the alumina surface and facilitate precipitation of iodinated species, such as aluminum iodate hexahydrate (AlH).

The experimental results reveal AlH decomposition was accompanied by continuous exothermic reaction, suggesting that the original alumina shell was replaced with AlH. Then, upon AlH decomposition, the pyrophoric Al core continuously oxidized and liberated heat. Another possibility is defects within the transformed shell facilitate oxygen diffusion to the core Al liberating heat throughout the equilibrium experiment. Both scenarios demonstrate the limiting effects of the alumina shell. These results indicate that through adsorption reactions more energy can be harnessed from iodine-species and alumina to (1) produce new passivation shell chemistry and/or (2) exploit exothermic surface reactions with Al particles.

Conflicts of interest

There are no conflicts to declare.

Acknowledgements

The authors are thankful for support from ARO grant W911NF-17-1-0387 and Dr. Ralph Anthenien. We are also grateful for support from ONR and DOE STEM grants N00014-21-1-2519 and NA0003988, respectively. Assistance from Dr. Daniel Unruh, Dr. Julio Warzywoda, Mr. Quan Tran, and Mr. Clayton Miller all from Texas Tech is thankfully acknowledged.

References

1 C. A. Crouse, C. J. Pierce and J. E. Spowart, *Combust. Flame*, 2012, **159**, 3199–3207.
2 H. A. Miller, B. S. Kusel, S. T. Danielson, J. W. Neat, E. K. Avjian, S. N. Pierson, S. M. Budy, D. W. Ball, S. T. Iacono and S. C. Kettwich, *J. Mater. Chem. A*, 2013, **1**, 7050–7058.
3 M. L. Pantoya and S. W. Dean, *Thermochim. Acta*, 2009, **493**, 109–110.
4 R. Padhye, D. K. Smith, C. Korzeniewski and M. L. Pantoya, *Appl. Surf. Sci.*, 2017, **402**, 225–231.
5 R. Padhye, A. J. A. Aquino, D. Tunega and M. L. Pantoya, *ACS Appl. Mater. Interfaces*, 2017, **9**, 24290–24297.
6 B. K. Little, S. B. Emery, J. C. Nittinger, R. C. Fantasia and C. M. Lindsay, *Propellants, Explos. Pyrotech.*, 2015, **40**, 595–603.
7 N. D. Williams and A. D. Russell, *J. Appl. Bacteriol.*, 1991, **70**, 427–436.
8 S. Banerjee, S. Zaghloul, A. Alaaeddine and B. Ameduri, *Polym. Chem.*, 2016, **7**, 6099–6109.
9 J. L. Gottfried, D. K. Smith, C.-C. Wu and M. L. Pantoya, *Sci. Rep.*, 2018, **8**, 8036.
10 C. W. Farley, M. L. Pantoya, M. Losada and S. Chaudhuri, *J. Chem. Phys.*, 2013, **139**, 074701.
11 O. Mulamba and M. Pantoya, *J. Nanoparticle Res.*, 2014, **16**, 2310.
12 H. Knözinger and P. Ratnasamy, *Catal. Rev.*, 1978, **17**, 31–70.
13 R. Padhye, A. J. A. Aquino, D. Tunega and M. L. Pantoya, *ACS Appl. Mater. Interfaces*, 2016, **8**, 13926–13933.
14 G. Kresse and J. Hafner, *Phys. Rev. B*, 1993, **47**, 558–561.
15 G. Kresse and J. Hafner, *Phys. Rev. B*, 1994, **49**, 14251–14269.
16 G. Kresse and J. Furthmüller, *Comput. Mater. Sci.*, 1996, **6**, 15–50.
17 G. Kresse and J. Furthmüller, *Phys. Rev. B*, 1996, **54**, 11169–11186.
18 G. Kresse and D. Joubert, *Phys. Rev. B*, 1999, **59**, 1758–1775.
19 J. P. Perdew, K. Burke and M. Ernzerhof, *Phys. Rev. Lett.*, 1996, **77**, 3865–3868.
20 R. Ahlrichs, M. Bär, M. Häser, H. Horn and C. Kölmel, *Chem. Phys. Lett.*, 1989, **162**, 165–169.
21 F. Weigend and R. Ahlrichs, *Phys. Chem. Chem. Phys.*, 2005, **7**, 3297.
22 F. Weigend, *Phys. Chem. Chem. Phys.*, 2006, **8**, 1057–1065.
23 K. A. Peterson, D. Figgen, E. Goll, H. Stoll and M. Dolg, *J. Chem. Phys.*, 2003, **119**, 11113–11123.
24 S. Grimme, J. Antony, S. Ehrlich and H. Krieg, *J. Chem. Phys.*, 2010, **132**, 154104.
25 D. K. Smith, D. K. Unruh, C.-C. Wu and M. L. Pantoya, *J. Phys. Chem. C*, 2017, **121**, 23184–23191.
26 D. K. Smith, D. K. Unruh, C.-C. Wu and M. L. Pantoya, *J. Phys. Chem. C*, 2017, **121**, 23184–23191.
27 P. D. Cradwick and A. S. de Endredy, *J. Chem. Soc., Dalt. Trans.*, 1977, **0**, 146–149.
28 I. Shancita, K. K. Miller, P. D. Silverstein, J. Kalman and M. L. Pantoya, *RSC Adv.*, 2020, **10**, 14403–14409.
29 J. Kalman, D. K. Smith, K. K. Miller, S. K. Bhattacharia, K. R. Bratton and M. L. Pantoya, *Combust. Flame*, 2019, **205**, 327–335.
30 R. J. Jouet, J. R. Carney, R. H. Granholm, H. W. Sandusky and A. D. Warren, *Mater. Sci. Technol.*, 2006, **22**, 422–429.
31 J. McCollum, M. L. Pantoya and S. T. Iacono, *J. Fluor. Chem.*, 2015, **180**, 265–271.
32 D. K. Smith, J. McCollum and M. L. Pantoya, *Phys. Chem. Chem. Phys.*, 2016, **18**, 11243–11250.
33 S. K. Bhattacharia, K. K. Miller, J. L. Gottfried and M. L. Pantoya, *J. DoD Res. Eng.*
34 J.C. Wren, G.A. Glowa, J. Merritt, *J. Nuclear Mat.* 1999, **265**, 161-177.
35 R.B. dos Santos, R. Rivelino, F. de Brito Mota, G.K. Gueorguiev, A. Kakanakova-Georgieva, *J. Phys. D: Appl. Phys*, 2015, **48**, 295104.
36 A. Kakanakova-Georgieva, G.K. Gueorguiev, R. Yakimova, E. Janzen, *J. Apply. Phys.* 2004, **96**(9), 5293-5297.